DEUTSCHES ELEKTRONEN-SYNCHROTRON

DESY SR 94-02
September 1994

X-ray Standing Waves in Noncentrosymmetric Crystals and the Phase Problem in Crystallography

B.N. Dev

Inst. of Physics, Sachivalaya Marg, Bhubaneswar, India

G. Materlik

Hamburger Synchrotronstrahlungslabor HASYLAB at DESY, Hamburg

ISSN 0723-7979

NOTKESTRASSE 85 - 22603 HAMBURG

To be sure that your preprints are promptly included in the
HIGH ENERGY PHYSICS INDEX,
send them to (if possible by air mail):

DESY
Bibliothek
Notkestraße 85
22603 Hamburg
Germany

DESY-IfH
Bibliothek
Platanenallee 6
15738 Zeuthen
Germany

DESY SR 94-02
SEPTEMBER 1994

X-ray standing waves in noncentrosymmetric crystals and the phase problem in crystallography

B.N. Dev[a] and G. Materlik[b]

[a]Institute of Physics, Sachivalaya Marg, Bhubaneswar 751005, India

[b]Hamburger Synchrotronstrahlungslabor HASYLAB at Deutsches Elektronen-Synchrotron DESY, Notkestr. 85, 22603 Hamburg, Germany

Abstract

The effect of the variation of f' and f'' on the phase of the x-ray standing wave field is discussed with the example of a semiforbidden GaAs(200) reflection and incident x-ray energies around Ga and As K edges. In noncentrosymmetric crystals the phases of the structure factors contribute to the phase of the standing wave field relative to lattice atoms in the unit cell. Generation of standing waves with $(00\,6)$ and $(00\bar{6})$ reflections in a $(00\,\bar{1})$ -cut $LiNbO_3$ crystal and detecting Nb fluorescence yield demonstrates how the phases of the structure factors $F(00\,6)$ and $F(00\bar{6})$ with respect to the origin at an Nb atom can be determined. The phase determination does not require the incident energy to be tuned very close to an absorption edge.

1. INTRODUCTION

X-ray standing waves are generated in large perfect crystals when a plane wave x-ray beam is diffracted from such crystals. The amplitude and the phase of the wave field are derived from the dynamical theory of x-ray diffraction. The phase of the wave field depends on the phase of the structure factor for the corresponding hkl reflection from the crystal.

The position of the antinodes (or nodes) of the standing wave field within the diffraction planar spacing in the crystal can be detected experimentally. This is to say that the phase of the standing wave field can be detected relative to the atoms in the unit cell as the antinodal (or nodal) position is determined by the phase. The phase of the structure factor is determined by measuring the phase shift introduced by the structure factor phase.

In the case of anomalous scattering the strong modifications of the dispersion parameters f' and f'' in the neighbourhood of an absorption edge of one element in the sample crystal causes a phase change in the structure factors. This phase change can be easily followed by x-ray standing wave (XSW) measurements, which identify the location of the diffraction planes within the unit cell.

---

published in:"Resonant Anomalous X-Ray Scattering. Theory and Applications", G. Materlik, C.J. Sparks & K. Fischer (eds.), Elsevier Science B.V., 1994, p. 119-143.

ISSN 0723-7979

The article has been arranged in the following way. In section 1 we discuss the phase problem in crystallography. Section 2 gives a brief description of the dynamical theory of x-ray diffraction, structure factor phases and anomalous dispersion. Experimental examples with GaAs(200) and $LiNbO_3$(006) and (00$\bar{6}$) are presented in section 3, which is followed by the conclusions in section 4.

2. THE PHASE PROBLEM

The crystal structure determination is equivalent to the determination of the electron density distribution in the unit cell. The complex scattering density function at a point **r** in the unit cell is given by

$$\rho(\mathbf{r}) = (1/V)\sum_H F_H \exp(-2\pi i \mathbf{H}\cdot\mathbf{r}), \quad \text{or} \tag{1.1}$$

$$\rho(\mathbf{r}) = (1/V)\sum_H |F_H| \exp(i(-2\pi \mathbf{H}\cdot\mathbf{r} + \beta_H)), \quad \text{where} \tag{1.2}$$

$$F_H = |F_H| \exp(i\beta_H) \tag{1.3}$$

is the structure factor and V is the volume of the unit cell. The summation runs over all reciprocal lattice points H.

The structure factor involves the strength of the elastic scattering and the relative positions of the scattering atoms in the unit cell, and is defined by

$$F_H = \sum_j f_j \exp(2\pi i \mathbf{H}\cdot\mathbf{r}_j)\exp(-M_j), \tag{1.4}$$

where f_j is the scattering factor of the jth atom, $\mathbf{r}_j$ its position vector and $\exp(-M_j)$ is the Debye-Waller factor for the jth atom in a unit cell containing N atoms. The atomic scattering factor f_j is given by

$$f_j = f_j^0 + f_j' + i f_j'', \tag{1.5}$$

where f_j' and f_j'' are the correction terms due to resonance scattering and absorption, respectively.

From Eq. (1.2) it is evident that $\rho(\mathbf{r})$, i.e., the structure, is readily determined if a complete set of structure factors - *in both magnitude and phase* - is available. In ordinary diffraction experiments the structure factor amplitudes, $|F_H|$, are determined, but not the phases, β_H, and this constitutes the *phase problem*. In the realm of the kinematical theory special techniques based on multiple-Bragg diffraction, anomalous dispersion, λ -method etc. have been used for the phase measurement. These methods are based on elastic scattering. However, with the dynamical scattering method the phase and the magnitude of each F_H can be measured by detecting an inelastic signal in addition to the elastic one.

3. DYNAMICAL THEORY OF X-RAY DIFFRACTION

The kinematical theory treats the scattering from each volume element in the sample as being independent of that of other volume elements. Darwin[1] was the first to notice this nonrigorous nature of the kinematical theory and introduce a dynamical theory. In his version of the dynamical theory of x-ray diffraction, Darwin introduced multiple reflection from the lattice planes involved in the diffraction. However, multiple scattering within a plane was neglected. In spite of the half-qualitative nature of his treatment, his theory made some important predictions which are in many aspects the same as the predictions of rigorous dynamical theories introduced by Ewald[2] and later by von Laue[3]. Ewald's theory is based on scattering by a periodic structure consisting of point resonators or dipoles. Laue regarded the crystal as a continuously distributed electron density with positive charges localized at the centers of the atoms. In Laue's approach the basic problem is to solve the Maxwell's equations in a medium with a periodic complex dielectric constant. In this section we present a brief description of Laue's theory, which has predominantly been used in x-ray diffraction.

3.1. Dynamical theory

Dynamical theory of x-ray diffraction has been discussed in details in several books[4-6]. There is an often used review article by Batterman and Cole[7] which brings out the physical aspects nicely. Here we briefly discuss the theory.

Propagation of a plane electromagnetic wave through a perfect crystal which can be considered neutral in the absence of an external field, produces displacements of negative charges and consequently gives rise to polarization, which in turn determines the effective field at any point $\mathbf{r}$ inside the crystal. The parameters that determine the wave field inside the crystal, such as dielectric constant $\epsilon(\mathbf{r})$ or electric succeptibility $\chi(\mathbf{r})$, must have the same periodicity as that of the crystal lattice. These parameters also should be complex in order to take the absorption of the electromagnetic waves into account. The wave field is determined by solving Maxwell's equations.

In the dynamical theory the electric displacement $\mathbf{D}$ (related to the electric field vector $\mathbf{E}$ by $\mathbf{D} = \epsilon \mathbf{E}$) at a point inside the crystal, is written as

$$\mathbf{D} = \exp(i\omega t)\exp(-2\pi i \mathbf{K}_0 \cdot \mathbf{r}) \sum \mathbf{D}_H \exp(-2\pi i \mathbf{H} \cdot \mathbf{r}), \tag{2.1}$$

where ω is the angular frequency of the incident radiation, $\mathbf{K}_0$ is the incident wave vector inside the crystal and $\mathbf{D}_H$ is the H-th Fourier component of $\mathbf{D}$. With the introduction of the Laue condition

$$\mathbf{K}_H = \mathbf{K}_0 + \mathbf{H}, \tag{2.2}$$

Eq. (2.1) can be written as

$$\mathbf{D} = \exp(i\omega t) \sum \mathbf{D}_H \exp(-2\pi i \mathbf{K}_H \cdot \mathbf{r}). \tag{2.3}$$

Eq. (2.3) describes the multiwave solution of the dynamical theory as contributions of an infinite number of plane waves with wave vectors K_H, which correspond to an infinite set of reciprocal lattice vectors H.

In most of the experiments on x-ray diffraction one deals with two beams - the incident beam and one diffracted beam corresponding to a single H. In this case Eq. (2.3) retains only two terms:

$$\mathbf{D} = \exp(i\omega t)[\mathbf{D}_0 \exp(-2\pi i \mathbf{K}_0 \cdot \mathbf{r}) + \mathbf{D}_H \exp(-2\pi i \mathbf{K}_H \cdot \mathbf{r})], \tag{2.4}$$

where $\mathbf{D}_0$ and $\mathbf{D}_H$ correspond to the incident and the diffracted beam respectively.

The ratio of the field amplitudes D_H/D_0, which depends on the angle of incidence of the plane wave x-ray beam and the orientation of the crystal surface with respect to the diffracting planes, can be expressed as

$$D_H/D_0 = -|b|^{1/2}\frac{|C|}{C}\left[\frac{F_H}{F_{\bar{H}}}\right]^{1/2} \cdot [\eta \pm (\eta^2 + b/|b|)^{1/2}], \tag{2.5}$$

where the normalized angular parameter

$$\eta = \eta' + i\eta'' = \frac{b\Delta\theta \sin 2\theta + (1/2)\Gamma F_0(1-b)}{\Gamma |C| |b|^{1/2} (F_H F_{\bar{H}})^{1/2}} \tag{2.6}$$

takes both aforementioned conditions into account:

$$\Delta\theta = \theta - \theta_B, \quad \text{(deviation from the Bragg angle)} \quad \text{and} \tag{2.7}$$

$$b = \cos\psi_0 / \cos\psi_H. \tag{2.8}$$

The definition of b for the Bragg geometry is explained in Figure 1 where φ, the asymmetry angle, is the angle between the crystal surface and the diffraction planes.

For the symmetric ($\varphi = 0$) Laue case b = +1, and for the symmetric Bragg case b = -1. η is a complex quantity because the structure factors F_H and $F_{\bar{H}}$ are in general complex. In Eq. (2.5) C is the polarization factor and is given by C = 1 for σ-polarization (D perpendicular to the plane of incidence) and $C = \cos 2\theta$ for π-polarization (D in the plane of incidence). In Eq. (2.6) $\Gamma = \lambda^2 r_e / \pi V$ with the classical electron radius r_e and V is the volume of the unit cell.

In what follows we shall restrict our discussion to the symmetric Bragg case. The ratio D_H/D_0 can be written in the polar form

$$D_H/D_0 = \left|\frac{D_H}{D_0}\right| \exp(i(\nu + \phi_H)), \tag{2.9}$$

where ν and ϕ_H are defined by the relations:

$$\eta \pm (\eta^2 - 1)^{1/2} = |\eta \pm (\eta^2 - 1)^{1/2}| \exp(i\nu), \tag{2.10}$$

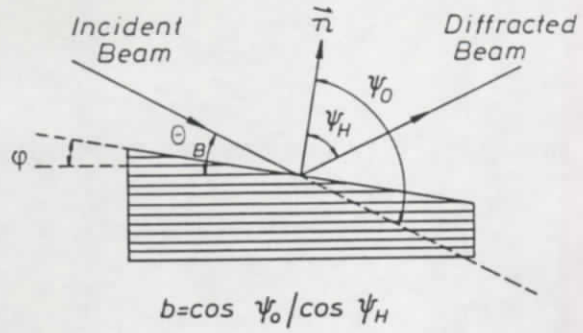

Figure 1. Asymmetrically cut crystal usually used in the monochromator to generate a quasi-plane wave incident x-ray beam.

and

$$\left(\frac{F_H}{F_{\bar{H}}}\right)^{1/2} = \left|\left(\frac{F_H}{F_{\bar{H}}}\right)^{1/2}\right| \exp(i(\beta_H - \beta_{\bar{H}})/2) = \left|\left(\frac{F_H}{F_{\bar{H}}}\right)^{1/2}\right| \exp(i\phi_H). \qquad (2.11)$$

The reflectivity is given by

$$R = |D_H/D_0|^2. \qquad (2.12)$$

The field intensity inside the crystal is, from Eq. (2.4)

$$I(\mathbf{r}, \Delta\theta) = \mathbf{D}^* \cdot \mathbf{D} = |D|^2 \qquad (2.13)$$

$$= |D_0|^2 \left[1 + \left|\frac{D_H}{D_0}\right|^2 + 2C\left|\frac{D_H}{D_0}\right| \cos(\nu + \phi_H - 2\pi\mathbf{H}\cdot\mathbf{r})\right] \exp(-\mu_z z),$$

where the effective attenuation coefficient $\mu_z = 4\pi K''_0$, $\mathbf{H} = \mathbf{K}_H - \mathbf{K}_0$ [from Eq. (2.2)] and z is the depth of the point represented by the position vector $\mathbf{r}$ measured from the crystal surface. Eq. (2.13) represents a standing wave solution.

For a centrosymmetric crystal, if the origin is chosen at a center of symmetry, and in the case of no absorption (i.e., $f'' = 0$), $|F_H| = |F_{\bar{H}}|$ and $\beta_H = -\beta_{\bar{H}} = 0$, i.e. $\phi_H = 0$ and the intensity is

$$I(\mathbf{r}, \Delta\theta) = |D_0|^2 \left[1 + \left|\frac{D_H}{D_0}\right|^2 + 2C\left|\frac{D_H}{D_0}\right| \cos(\nu - 2\pi\mathbf{H}\cdot\mathbf{r})\right] \exp(-\mu_z z). \qquad (2.14)$$

Within the angular region of strong reflectivity ν varies from π to 0 as the angle of incidence advances across the reflection, and

$$\nu = \pi \quad for \quad \eta' \geq 1,$$

$$\nu = 0 \quad for \quad \eta' \leq -1. \tag{2.15}$$

From Eq. (2.14), the condition for an antinode (i.e. the maximum intensity) is:

$$\nu - 2\pi \mathbf{H}\cdot\mathbf{r} = \pm n\pi \quad , \quad n = 0,2,4,\ldots \quad . \tag{2.16}$$

For $\nu = \pi$ the antinodes are at $r_H = [(1 \pm n)/2]d_H$ and for $\nu = 0$ the antinodes are at $r_H = \pm(n/2)d_H$. (r_H is the component of $\mathbf{r}$ in the direction of $\mathbf{H}$. That is, $\mathbf{H}\cdot\mathbf{r} = r_H/d_H; d_H = 1/|\mathbf{H}|$.)

That is, at the high angle side, where $\nu = 0$, an antinode coincides with the origin. However, if the structure factor has a nonvanishing phase ($\beta_H \neq 0$), which is in general true for noncentrosymmetric and absorbing crystals, the condition for the antinode is

$$\nu + \phi_H - 2\pi \mathbf{H}\cdot\mathbf{r} = 0 \quad (\text{for } n = 0), \tag{2.17}$$

$$\text{i.e.,} \quad r_H = \frac{\nu + \phi_H}{2\pi} d_H. \tag{2.18}$$

For an absorbing crystal there is no region of total reflection, and the phase ν varies continuously and is no longer constant for $|\eta'| \geq 1$. However, the asymptotic limits of ν can be determined. It can be shown that

$$\lim_{\eta' \to \infty} \nu = \pi + \frac{\beta_H + \beta_{\bar{H}}}{2}, \tag{2.19a}$$

and

$$\lim_{\eta' \to -\infty} \nu = \frac{\beta_H + \beta_{\bar{H}}}{2}, \tag{2.19b}$$

These yield the limiting values of $\nu + \phi_H$:

$$\lim_{\eta' \to \infty} \nu + \phi_H = \pi + \frac{\beta_H + \beta_{\bar{H}}}{2} + \frac{\beta_H - \beta_{\bar{H}}}{2} = \pi + \beta_H, \quad \text{and} \tag{2.20a}$$

$$\lim_{\eta' \to -\infty} \nu + \phi_H = \beta_H. \tag{2.20b}$$

The positions of the antinodes are therefore, from Eq. (2.16), (2.17) and (2.18), at $[(1 \pm n)/2 + \beta_H/2\pi]d_H$ and $(\pm n/2 + \beta_H/2\pi)d_H$ for $\eta' \to \infty$ and $\eta' \to -\infty$, respectively. At $\eta' \to -\infty$ the positions of the antinodes coincide with those of the diffraction planes [8].

Therefore, the detection of the position of the antinode with respect to an origin in the unit cell (for example, a particular atom) enables one to determine β_H. The position of the antinode can be detected easily by monitoring a secondary process (e.g. fluorescence) which, in the dipole approximation, is proportional to the field intensity on the fluorescing atom.

3.2. Phase measurements with dynamical diffraction

In this section we shall discuss the phases of crystal structure factors with reference to two systems, namely GaAs and $LiNbO_3$. We shall write down explicit structure factors, which will be used to explain experimental results presented in section 4.

3.2.1. GaAs(200)

In this section it will be demonstrated, based on the work in Ref. 8, that the changes in the phase of the structure factors due to anomalous scattering can be followed by the x-ray standing wave (XSW) technique. When the incident x-ray energy is in the vicinity of the absorption edge of a constituent element in the crystal, the dispersion parameters f' and f'' in the atomic form factor f of the relevant type of atoms are strongly modified, which in turn modifies the structure factors [confer Eq. (1.4) and (1.5)]. While performing an XSW experiment with a particular hkl reflection the structure factors $F(hkl)$ and $F(\bar{h}\bar{k}\bar{l})$ determine the electric field amplitude inside the crystal, and their phases determine the periodic position of the antinodes of the standing wave field in the crystal [Eq. (2.18)]. The periodic position of the antinodes can be determined by detecting a secondary signal, such as, photoelectron or fluorescence from any type of atoms in the crystal. We shall discuss the experimental procedure and results in section 4.

Let us take the example of a GaAs crystal. The projection of the atomic positions in the $(0\bar{1}1)$ plane is illustrated in Figure 2. In a reference system where the Ga atoms in the unit cell are at positions (000) + fcc and the As atoms at positions (1/4,1/4,1/4) + fcc, the complex structure factor $F_H = F'_H + iF''_H$ for a (111) and a (200) reflection become:

$$F_{(111)} = 4(f^0_{Ga} + f'_{Ga} + f''_{As}) - i4(f^0_{As} + f'_{As} - f''_{Ga}); \qquad (2.21a)$$

$$F_{(200)} = 4(f'_{Ga} - f'_{As} + f^0_{Ga} - f^0_{As}) + i4(f''_{Ga} - f''_{As}). \qquad (2.21b)$$

The phase of a structure factor F_H is defined by:

$$\beta_H = \tan^{-1}(F''_H / F'_H). \qquad (2.22)$$

The phases of the structure factors $F(111)$, $F(\bar{1}\bar{1}\bar{1})$, $F(200)$ and $F(\bar{2}00)$ are thus given by

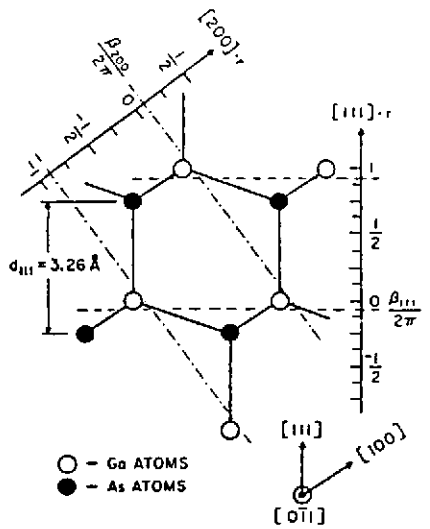

Figure 2. Structure of GaAs.

$$\beta_{\pm(111)} = \mp \tan^{-1} \frac{(f^0_{As} + f'_{As} \mp f''_{Ga})}{(f^0_{Ga} + f'_{Ga} \pm f''_{As})}, \tag{2.23}$$

and

$$\beta_{\pm(200)} = \tan^{-1} \frac{(f''_{Ga} - f''_{As})}{(f^0_{Ga} + f'_{Ga} - f^0_{As} - f'_{As})}. \tag{2.24}$$

Before we discuss the dependence of the phase on f' and f'' of the constituent elements in the GaAs crystal and their role in determining the position of the diffraction planes, let us discuss a simple case, namely, Ge with no absorption.

The schematic structure of GaAs is shown in Figure 2. For a Ge crystal all the Ga and As atoms would be replaced by Ge. Then from Eq. (2.23), we obtain

$$\beta_{\pm(111)} = \mp \tan^{-1} \frac{f^0_{Ge} + f'_{Ge} \mp f''_{Ge}}{f^0_{Ge} + f'_{Ge} \pm f''_{Ge}}. \tag{2.25}$$

With $f''_{Ge} = 0$ in the case of no absorption:

$$\beta_{\pm(111)} = \mp \frac{\pi}{4}. \tag{2.26}$$

This phase depends on the choice of origin. Here the origin has been chosen to be on a Ge atom on the upper layer of the (111) Germanium bilayers (identical to a Ga site as shown in Fig. 2). If the origin were chosen to be at the midpoint of a Ge-Ge bond in a bilayer, one would obtain $\beta_{(111)} = 0$. These different choices of origin leading to different phase values of the structure factors do not change the relative positions between the antinodal planes and the atomic planes. For example in the first case, the position of an antinode, from Eq. (2.11), (2.15) and (2.18), for $\eta' = -1$ (i.e. $\nu = 0$) is at

$$r_{(111)} = -\frac{1}{8} d_{111} \quad , \tag{2.27}$$

and with the second choice of origin at

$$r_{(111)} = 0 \quad . \tag{2.28}$$

Both these positions in the respective coordinate systems indicate a plane halfway between the Ge-Ge bond in the bilayer.

The phase defined so far for Ge is purely of geometric origin. Now, let us introduce the absorption parameter f''_{Ge}. The modification thus introduced in the structure factor F_{111} is shown schematically in Fig. 3. The phase of the structure factor thus obtained is $\beta_H^{(1)}$. Near an absorption edge f''_{Ge} also will change to $f''^{(2)}_{Ge}$ ($f''^{(2)}_{Ge} < f''_{Ge}$) which in turn will change the structure factor with the new phase $\beta_H^{(2)}$. The phase changes from β_H to $\beta_H^{(1)}$ or to $\beta_H^{(2)}$ are purely due to the elastic scattering process and are *not of geometric origin*. These phase changes will shift the positions of the antinodes with respect to the atomic positions in the unit cell. The antinodal planes approach the diffraction planes for $\eta' \to -\infty$. This means that there is an energy dependent shift of the position of the diffraction planes even in centrosymmetric crystals.

For GaAs(200), one sees from Eq. (2.21b) that (200) is a "semiforbidden" reflection as differences of nearly equal quantities: $f'_{Ga} - f'_{As}$, $f^0_{Ga} - f^0_{As}$ and $f''_{Ga} - f''_{As}$ make both F'_{200} and F''_{200} almost zero. These differences can be drastically modified near the absorption edges of Ga and As leading to a dramatic variation in the phase value $\beta_*(200)$. Fig. 4 shows the f' and f'' values of Ga and As near their absorption edges with the computed $\beta_{(200)}$ [from Eq. (2.24)]. These phase variations have been monitored in x-ray standing wave experiments, which will be discussed later.

3.2.2. $LiNbO_3(006)$ and $(00\bar{6})$

The case of $LiNbO_3$ is being presented as our original work which has not been published before. $LiNbO_3$ crystal has been chosen for the phase measurement for the following reasons.

(a) At room temperature $LiNbO_3$ has no centre of symmetry (space group R3c).

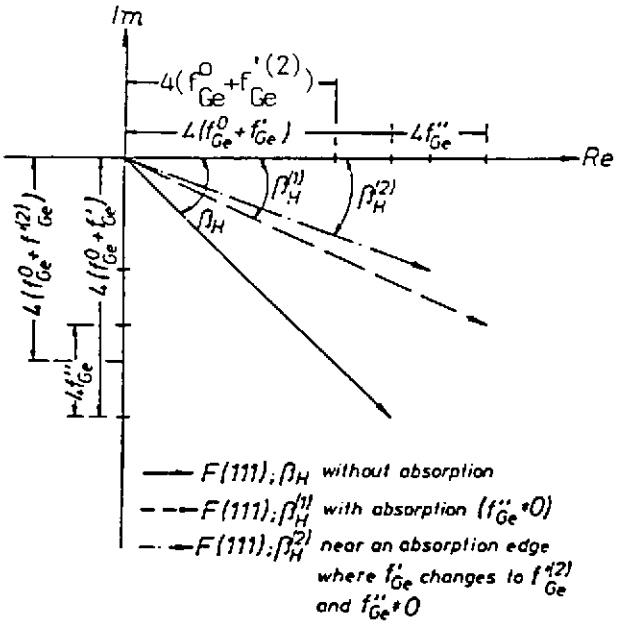

Figure 3. Phase variation of structure factors with changes in the anomalous dispersion parameters is shown in the complex plane.

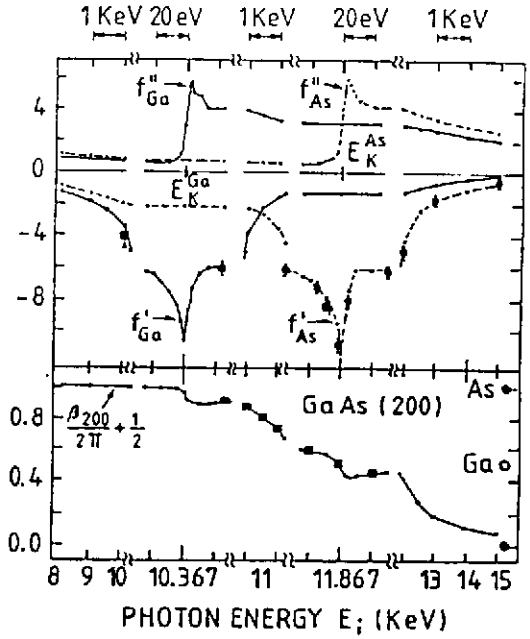

Figure 4. Variation of the anomalous dispersion parameters f' and f" for Ga and As atoms around their K absorption edges. The variation of the phase $\beta_{(200)}$ of the GaAs(200) structure factor with energy is also shown.

(b) The quality of crystal perfection is usually much worse (more strain, higher dislocation density) than that of the so-called perfect crystals - Si, Ge, GaAs, GaP etc.

Because of reasons (a) and (b) $LiNbO_3$ represents a general case and has been chosen for a demonstration of the structure factor phase measurement using x-ray standing waves.

Other reasons for chosing $LiNbO_3$ are:

(c) $LiNbO_3$ undergoes a phase transition, ferroelectric (R3c) to paraelectric ($R\bar{3}c$), at 1210°C with displacement of the Nb and Li atoms. Thus it offers the possibility of studying the applicability of x-ray standing waves to bulk phase transition problems.

(d) $LiNbO_3$ has tremendous practical applications, Ti-diffused $LiNbO_3$ being the most widely used material for ferroelectric optical-waveguide device fabrication. Nevertheless, very little is known about the Ti position in the $LiNbO_3$ lattice and how it correlates with the optical properties. Fe-diffused $LiNbO_3$ bears great potential as optical storage medium. The location of these impurities can be precisely determined by the x-ray standing wave methods.

The structure of $LiNbO_3$ is known. The unit cell (space group R3c) can be described in rhombohedral or hexagonal coordinates. Here we will use the hexagonal coordinate system. The unit cell contains six $LiNbO_3$ molecular units, i.e., six Nb, six Li and eighteen O atoms. The general coordinates are:

$$(0,0,0;\ 1/3,2/3,2/3;\ 2/3,1/3,1/3)+|x,y,z;\bar{y},x-y,z;$$

$$y-x,\bar{x},z;\ \bar{y},\bar{x},1/2+z;\ x,x-y,1/2+z;\ y-x,y,1/2+z|.$$

Choosing the origin at an Nb atom, we get

$$\begin{aligned} &Nb:\ x=0,\ y=0,\ z=0; \\ &Li:\ x=0,\ y=0,\ z=Z_{Li}; \\ &O:\ x=X_0,\ y=Y_0,\ z=Z_0; \end{aligned} \tag{2.29}$$

where $Z_{Li}=0.2829$,

and $X_0=0.0492$; $Y_0=0.3446$; $Z_0=0.0647$. (2.30)

The structure factor $F(hkl)$ is given as [Eq. (1.4)]:

$$F(hkl)=\sum f_j(hkl)\exp[2\pi i(hx_j+ky_j+lz_j)]\exp(-M_j), \tag{2.31}$$

where j runs over all the atoms in the unit cell.

The structure factors for the (006) and $(00\bar{6})$ reflections can be written as

$$\begin{aligned} F(006)=&\{(f^0_{Li}+f'_{Li})A_{Li}+(f^0_{Nb}+f'_{Nb})A_{Nb}+(f^0_O+f'_O)A_O-f''_{Li}B_{Li}-f''_OB_O\} \\ &+i\{(f^0_{Li}+f'_{Li})B_{Li}+(f^0_O+f'_O)B_O+f''_{Li}A_{Li}+f''_{Nb}A_{Nb}+f''_OA_O\}, \end{aligned} \tag{2.32}$$

$$\begin{aligned} F(00\bar{6})=&\{(f^0_{Li}+f'_{Li})A_{Li}+(f^0_{Nb}+f'_{Nb})A_{Nb}+(f^0_O+f'_O)A_O+f''_{Li}B_{Li}+f''_OB_O\} \\ &-i\{(f^0_{Li}+f'_{Li})B_{Li}+(f^0_O+f'_O)B_O-f''_{Li}A_{Li}-f''_{Nb}A_{Nb}-f''_OA_O\}, \end{aligned} \tag{2.33}$$

where

$A_{Nb}=6$, $A_{Li}=6\cos(12\pi Z_{Li})$, $B_{Li}=6\sin(12\pi Z_{Li})$, $A_O=18\cos(12\pi Z_O)$ and $B_O=6\sin(12\pi Z_O)$.

The phase of $F(006)$ and $F(00\bar{6})$ are given by

$$\beta_{*(006)}=\pm\tan^{-1}\frac{(f^0_{Li}+f'_{Li})B_{Li}+(f^0_O+f'_O)B_O\pm f''_{Li}A_{Li}\pm f''_{Nb}A_{Nb}\pm f''_OA_O}{(f^0_{Li}+f'_{Li})A_{Li}+(f^0_{Nb}+f'_{Nb})A_{Nb}+(f^0_O+f'_O)A_O\mp f''_{Li}B_{Li}\mp f''_OB_O}. \tag{2.34}$$

In these expressions the Debye-Waller factor $\exp(-M_j)$ has been absorbed in the definition of f_j.

For an incident x-ray beam of energy E_γ = 8.3 keV,

$$f_{Li}^0 = 1.70 \quad , \quad f_{Nb}^0 = 31.44 \quad , \quad f_0^0 = 5.46;$$

$$f_{Li}' = -5.91E-05 \quad , \quad f_{Nb}' = -0.29 \quad , \quad f_0' = 4.29E-02; \tag{2.35}$$

$$f_{Li}'' = 3.12E-04 \quad , \quad f_{Nb}'' = 2.35 \quad , \quad f_0'' = 3.02E-02.$$

These values were calculated using the formulas of Cromer and Liberman[9]. By multiplying these values with appropriate Debye-Waller factors[10]: $\exp(-M_{Li}) = 0.957$, $\exp(-M_{Nb}) = 0.977$ and $\exp(-M_O) = 0.980$, and using them in Eqs. (2.31), (2.32) and (2.33) one gets the computed structure factor values:

$$F(000) = 404.18 \quad \exp(i0.0363),$$

$$F(006) = 127.12 \quad \exp(i0.5624), \quad \text{and} \tag{2.36}$$

$$F(00\bar{6}) = 115.74 \quad \exp(-i0.3621).$$

Use of the interpolated values of f^0, f' and f'' from the tabulated values at given energies in the International Tables of X-ray Crystallography leads to 2 % and 4 % smaller values of phase for $F(006)$ and $F(00\bar{6})$, respectively. The computed phases of D_H/D_0 for (006) and (00$\bar{6}$) reflections and the phase of $[\eta \pm (\eta^2 - 1)^{1/2}]$ as a function of the real part of the reduced angular parameter η are shown in Figure 5. The asymptotic values of the phases are attained at $|\eta'| \cong 200$. However, it is seen from the figure that the phase variation beyond $|\eta'| > 1$ is very slow - especially slow beyond $|\eta'| > 3$.

The field intensities at $\mathbf{r} = 0$, i.e. at the Nb site, can be calculated using Eq. (2.13). These are shown in Figure 6 for two different incident x-ray energies - one above and the other below the Nb K edge. The field intensity profile can be measured by detecting a process proportional to the field intensity, e.g. fluorescence yield, from an atom at $\mathbf{r} = 0$. Therefore the phase of the structure factor of the corresponding reflection, used in the experiment, can be measured.

This method can provide a set of phases $\{\beta_H\}$ with respect to the origin at the fluorescing atom. The value of β_H depends on the choice of origin. If we refer to another origin, we simply add an extra phase with β_H. This is obvious from Eq. (1.4). Substituting $\mathbf{r} = \mathbf{r}^n + \mathbf{a}$ in Eq. (1.4) we obtain $F_H^n = F_H \exp(-2\pi i \mathbf{H}\cdot\mathbf{a})$, where F_H^n is the structure factor with respect to the origin, which is at $\mathbf{a}$ with respect to the old origin. The effect of this is to multiply D_H/D_0 [Equ. (2.5)] by the factor $\exp(-2\pi i \mathbf{H}\cdot\mathbf{a})$. Therefore

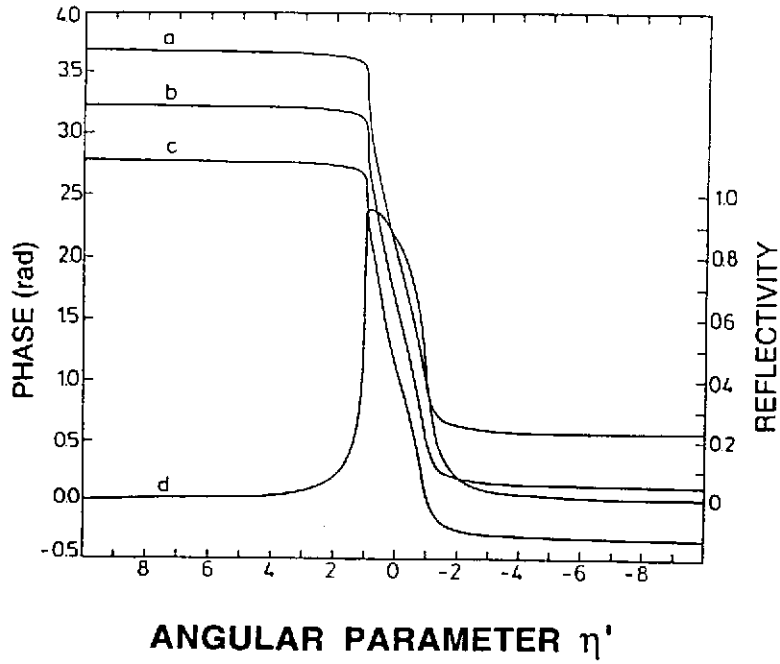

Figure 5. Variation of the phase $\nu + \Phi_H$ as a function of η' at E_γ = 8.3 keV. (a) for (006); (b) the phase of $\eta \pm (\eta^2 - 1)^{1/2}$, i.e. ν and (c) for $00\bar{6}$. (d) (006) reflectivity.

the phase with respect to the new origin $\beta_H^n = \beta_H - 2\pi \mathbf{H} \cdot \mathbf{a}$. The charge density calculated from the new set of phases $\{\beta_H^n\}$ will be identical to that calculated from the set $\{\beta_H\}$.

In an XSW experiment, if the inelastic signals from more than one type of atom are detected, information about their relative positions can be obtained directly. The (006) and ($00\bar{6}$) reflectivity and, in both cases, the field intensities at the Nb site and the O site are shown in Figure 7. These shapes of the field intensities can be simultaneously measured by measuring, say, O and Nb fluorescence yields simultaneously. The plots shown in Figure 7 are for an incident x-ray energy of 8 keV.

Now we will discuss some advantages of making measurements at lower energies. As we notice from figures 6 and 7, the angular width of the reflectivity curve is smaller at higher energies compared to that at lower energies. Most of the single crystals usually have a mosaic spread. If the mosaic spread in angle is comparable to or larger than the theoretical width of the rocking curve, dynamical effects will be washed out. In this situation, using x-rays of lower energy the natural rocking curve width can be increased so that mosaic spread is now smaller than the reflectivity width. In this situation the crystal is expected to show dynamical behaviour.

A second problem is associated with the energy of the detected fluorescence photon. We will compare the cases with E_γ = 20 keV and E_γ = 8 keV. At 20 keV we are above the Nb K-edge. In this situation one can detect Nb L photons as well as Nb K photons. However, the cross section for Nb L photoionization and radiative transitions are much smaller compared to Nb K and leads to a

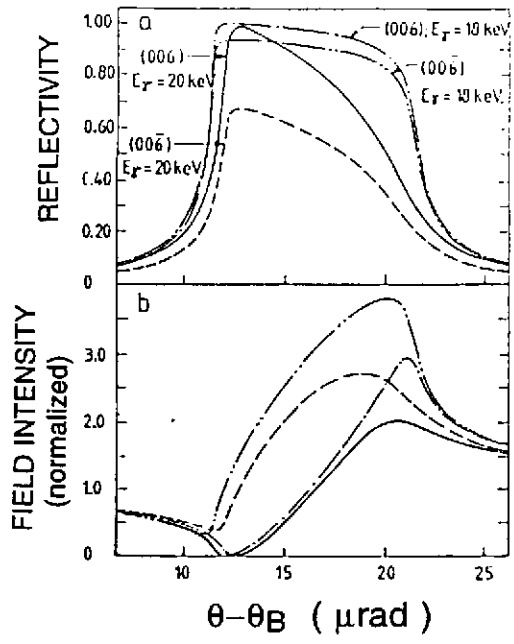

Figure 6. a) Reflectivity and b) the standing wave field intensity at the Nb site at two different incident energies - below and above the Nb K-edge. In (b) (- - -) and (– · · –) are the field intensities for 18 keV x-rays for (006) and 00$\bar{6}$ reflections, respectively. (___) and (---) are the corresponding results for 20 keV.

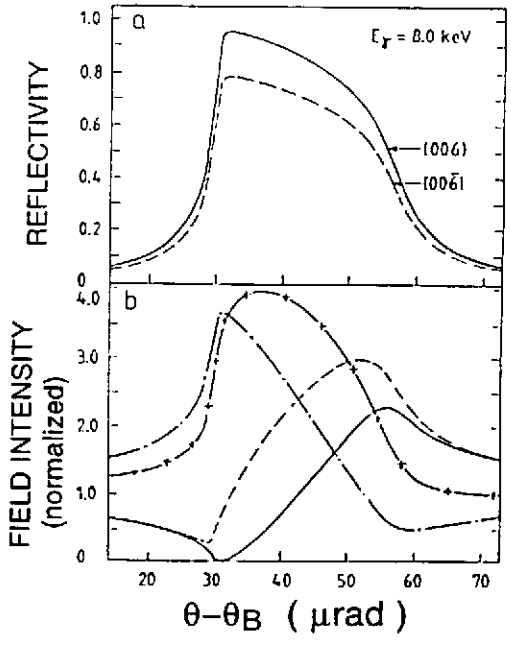

Figure 7. Theoretical (a) reflectivities and (b) the standing wave field intensities at the Nb and the O sites. (___) and (---) are the field intensities at the Nb site and (-+-) and (– · –) are the field intensities at the O site for (006) and (00$\bar{6}$) reflections, respectively.

very small yield of Nb L fluorescence. To increase the yield of Nb L fluorescence one needs to perform an experiment with an incident energy above and near the Nb L absorption edge. At 20 keV incident energy Nb K fluorescence yield is very large. However, the high energy ($E_{K\alpha}$ = 16.58 keV) of the fluorescence photons leads to a strong extinction effect, which is a function of the angle (α) between the sample surface and the detector. In figures 6 and 7 the field intensities at different sites are shown. These are valid only for atoms in the surface region. As the incident x-ray beam penetrates into the crystal there is an exponential damping of the intensity which is taken care of by the factor $\exp(-\mu_z z)$ in Eq. (2.13) where z is the depth from the surface into the crystal. μ_z has an angular dependence within the region of reflection:

$$\mu_z(\theta) = \frac{\mu_0}{\sin\theta_B}\left[1 + C\left(\frac{F_{\bar{H}}}{F_0}\right)\left(\frac{D_H}{D_0}\right)^{'} + C\left(\frac{F_{\bar{H}}}{F_0}\right)\left(\frac{D_H}{D_0}\right)^{''} \right]. \qquad (2.37)$$

A secondary signal (e.g. fluorescence, photoelectron, Auger electron etc.) generated in an atom at a depth z also suffers absorption in coming out of the sample. Both the effects of the primary and secondary extinctions can be accounted for in estimating the angular dependence of the secondary signal yield by multiplying the unattenuated field intensity by a quantity z_{eff} given by [8,17]:

$$z_{eff} = [\mu_z(\theta) + \mu_{out}/\sin(\alpha)]^{-1}, \qquad (2.38)$$

where μ_{out} is the linear attenuation coefficient for the outgoing secondary signal, and α is the angle between the secondary signal detector and the sample surface.

For 20.0 keV incident photon and for (006) reflection (d = 2.31 Å):

$$\mu_0 = 225.71 \ \ cm^{-1} \ , \ \mu_z(\text{Off-Bragg}) = \mu_0/\sin\theta_B, \qquad (2.39)$$

$$\mu_z(\eta' = 0) = 10247 \ \ cm^{-1}. \qquad (2.40)$$

When Nb K_α (E_{out} = 16.58 keV) is detected

$$\mu_{out} = 58.17 \ \ cm^{-1}. \qquad (2.41)$$

In Figure 8 we see the effect of the variation on α. Even for a value as small as 1° the distortion of the fluorescence angular yield is very large. This poses a problem for accurate phase determination because for a large α the angular variation of the Nb K_α yield for (006) and $(00\bar{6})$ reflections may look very similar. This poses a problem when the orientation is not known.

At 8.0 keV incident photon energy

$$\mu_0 = 428.85 \ \ cm^{-1} \ , \ \mu_z(\eta' = 0) = 11163 \ \ cm^{-1}. \qquad (2.42)$$

If we detect Nb L fluorescence photons, $E_{L\alpha 1}$ = 2.166 keV, $E_{L\alpha 2}$ = 2.163 keV and $E_{L\beta 1}$ = 2.257 keV cannot be separated with a Si(Li) detector resolution. The strongest lines are L_α, and $L_{\beta 1}$, the energies of which are below all L absorption edges ($E_{L_{III}}$ = 2.371 keV, $E_{L_{II}}$ = 2.464 keV, E_{L_I} = 2.71 keV). Thus the absorption coefficient for the Lα and Lβ energies should be very similar. We use the absorption coefficients for E_{out} = 2.26 keV in the calculation. At 2.26 keV

$$\mu_{out} = 2585.6 \ \ cm^{-1}. \qquad (2.43)$$

In this case the fluorescence yield angular variation (Figure 9) is not as sensitive to α as it is when Nb K_α fluoresence photons are detected.

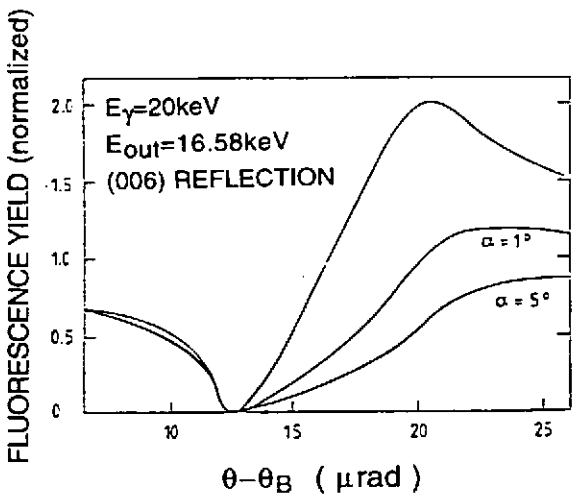

Figure 8. Theoretical curves showing the effect of extinction on the detected NbK_α fluorescence yield. α-dependence is very strong. The top curve is obtained without taking any extinction into account.

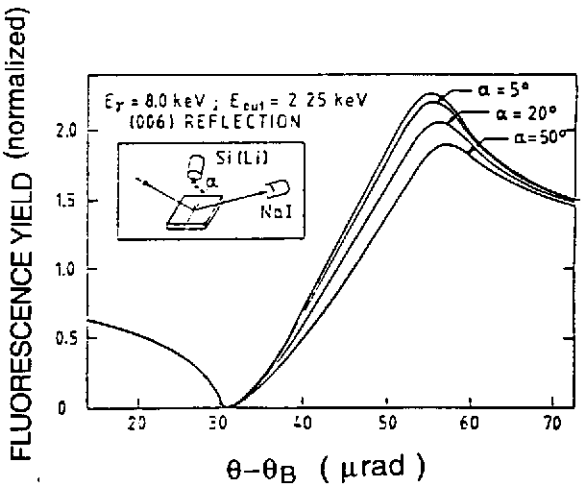

Figure 9. Theoretical curves showing the effect of extinction on the detected Nb L fluorescence yield. Dependence on the angle between the sample surface and the Si(Li) detector, α, is small. The top curve corresponds to no-extinction effect.

4. Experimental Examples

In this section we will first describe how to carry out an XSW experiment and how a synchrotron radiation source is particularly helpful in carrying out such experiments. Then we will give examples of the topics discussed in section 3.

4.1. How to carry out an XSW experiment

A typical XSW experimental set-up is shown in Figure 10. The main components are:

(i) An x-ray source, which can be a sealed x-ray tube, a rotating anode x-ray source or a synchrotron radiation source.
(ii) A monochromator, which can be a single or a multicrystal assembly.
(iii) A detector, usually a NaI scintillation detector or an ionization chamber, for detecting the diffracted beam and measuring its intensity.
(iv) An energy dispersive Si(Li) detector to detect fluorescence photons from different atomic species or an electron detector.

(v) A fine angle control device for rocking the sample crystal within a small angular region. This is usually attained by using the small expansion of a piezoelectric crystal upon application of a high voltage (≅ 1000 V) and transforming the linear displacement into an angular displacement through a mechanical device.

(vi) A multichannel analyzer to record the Si(Li) energy spectrum.

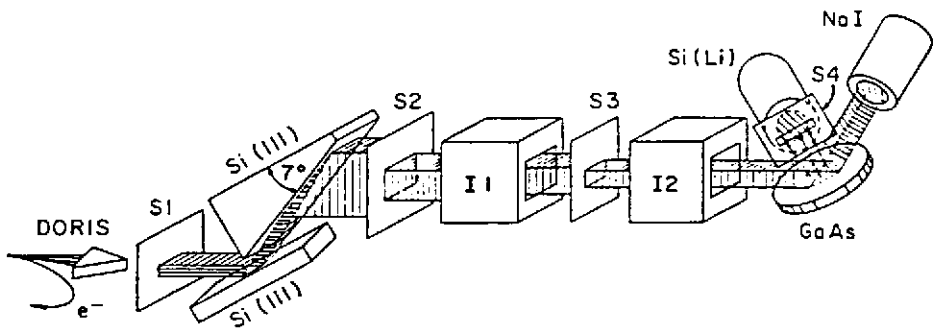

Figure 10. A schematic view of the experimental set-up of the ROEMO experimental station at HASYLAB.

The items (i) to (vi) just gives a guideline about the requirements. There are indeed many more possible configurations.

In Figure 10 the slits S1, S2 and S3 are to restrict the beam over a certain region. The position of the slit S4 in front of the Si(Li) detector selects the angle α, mentioned in the previous section. The ionization chambers I1 and I2 detect x-rays and measure their intensities. The asymmetrically-cut crystal in the double crystal monochromator assembly collimates the beam which is already monochromatized by the first crystal. The monochromatized and collimated beam is a good approximation to the plane wave used in the theory. The sample crystal (here GaAs) is first set to a Bragg angle to obtain the diffracted beam in the NaI detector. Then the sample is rocked back and forth with the piezo device to obtain the rocking (reflectivity) curve. This requires simultaneous measurements of the reflectivity and of the corresponding inelastically scattered photon energy spectrum in the Si(Li) detector for a particular angle. With this brief description about the experiments let us discuss the results of experiments on a few systems.

4.2.1. GaAs(200)

When there is no phase contribution from the structure factors (i.e. $\phi_H = 0$) we notice from Eqs. (2.15) and (2.18) that at the angle of incidence corresponding to $\eta' = 1$ (i.e., $\nu = \pi$) the antinodes are halfway between the diffraction planes. As the angle of incidence increases η' continuously goes to zero and decreases further. The antinodes move inwards and finally when

$\eta' < -1$ the antinodes coincide with the diffraction planes. That is, as the angle of incidence is increased a given atom in the crystal is exposed to different field intensities. If the position of this atom coincides with the position of the diffraction plane, the intensity on that atom will be maximum for the high angle edge ($\eta' = -1$) of the reflectivity curve and minimum at the low-angle edge ($\eta' = 1$). Thus the fluorescence signal will peak on the high-angle edge. As we have discussed in section 3, the diffraction plane position varies with the variation of f' and f". In that case the shape of the fluorescence yield angular profile also changes.

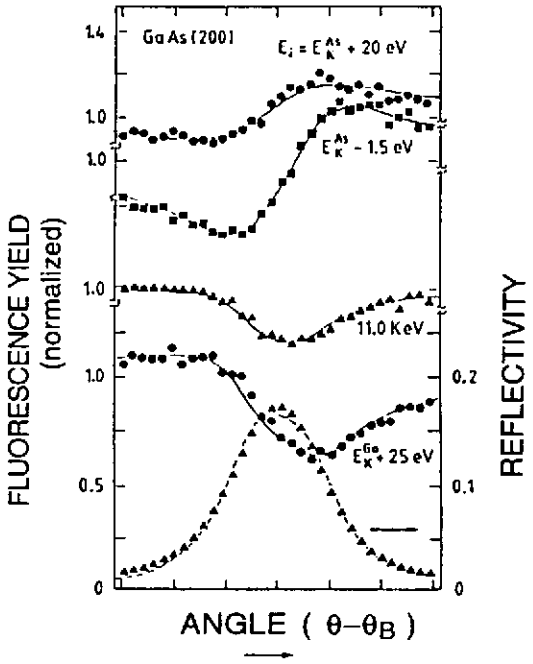

Figure 11. Reflectivity and Ga K_α fluorescence yield variation with the angle of incidence at different incident energies around the Ga and As K-edges. The angular range for each XSW scan was ≅ 50 μrad.

Figure 11 shows the reflectivity and the Ga K_α yield for a GaAs(200) reflection. From Figure 4 we notice that depending on the incident energy the phase β_{200} can vary approximately within the region from π to $-\pi$. Figure 11 shows four Ga K_α fluorescence yield profiles. For the measurement at E_K^{Ga} + 25 eV, $\beta_{200} \cong 0.8\pi (\beta_{200}/2\pi + 1/2 \cong 0.9)$. This makes the antinodal planes move from $r_H = 0.9\ d_H$ to $r_H = 0.4\ d_H$ as the angle of incidence advances across the rocking curve, resulting in high Ga K_α fluorescence yield at the low angle side. At an incident photon energy of 11.0 keV the antinodal plane movements are from $0.8\ d_H$ to $0.3\ d_H$,that is, both at the low-angle side and the high-angle side Ga atoms are approximately at the same distance from the nearest antinodal planes. This gives rise to almost equal yields on both low-angle and the high-angle sides. For $E_i = E_K^{As} - 1.5eV$, $\beta_{200} = 0$ and the antinodes coincide with the Ga atoms on the high-angle side giving rise to

high Ga Kα fluorescence yield. Beyond this incident energy, all the anomalous dispersion effect gradually diminishes and the modulation in the fluorescence yield becomes very weak. This is evident from the measurement at $E_i = E_K^{As} + 20eV$. This example nicely explains how the anomalous dispersion parameters f'_{Ga}, f''_{Ga}, f'_{As} and f''_{As} have affected the diffraction plane position with respect to atomic coordinates in a unit cell. Of course for a known structure this mode of measurement can also be used to determine f' and f'' as a function of λ. The tunability of the energy of the synchrotron x-radiation makes these measurements possible.

4.2.2. $LiNbO_3$ (006) and $(00\bar{6})$

The experiments that will be discussed in this section have been performed at the ROEMO experimental station of the Hamburg Synchrotron Radiation Laboratory HASYLAB at DESY. The experimental set up was very similar to the one shown in Figure 10. The first crystal in the monochromator was a Ge(220) and the second was an asymmetrically cut Si(220) crystal. For an XSW experiment one should preferably use a nondispersive set up, i.e., the monochromator and the sample crystal in the (+,-) configuration and the d_{hkl} corresponding to the monochromator reflection should be the same as that for the reflection from the sample crystal. This basically means using the same material for the monochromator and the sample with the same (hkl) reflection from both. However, perfect enough $LiNbO_3$ crystals were not available for use as a monochromator. Our monochromator sample combination is slightly dispersive. For Si, d_{220} = 1.92 Å and for $LiNbO_3$, d_{006} = 2.31 Å. Dispersion effects have been taken into account in the analyses of the reflectivity, the fluorescence yield and the electron yield profile.

The quality of available $LiNbO_3$ crystals is usually much worse than that of good quality crystals like Si, Ge, GaAs etc. It is necessary to select a reasonably good region of the sample by topographic methods. Prior to an XSW experiment, topography [11] is routinely done even on good crystals like Si and Ge in order to detect and avoid strained regions. Some topograms of $LiNbO_3$ are shown in Figure 12. In fact, topograms revealed dislocations, strain and twinning in the $LiNbO_3$ single crystals. With the help of the topograms reasonably perfect regions of the crystal were selected through the S3 slit system (Figure 10) for the XSW experiment.

Figure 13 shows the structure[12-15] of $LiNbO_3$ [c = 13.8620 Å, a = 5.1494 Å] with the (006) planar spacing and the $(00\bar{6})$ diffraction planes. The position of the $(00\bar{6})$ diffraction planes varies slightly with incident energy because of anomalous dispersion. This will be explained later with examples at 18 and 20 keV (E_K^{Nb} = 18.99 keV) incident x-rays.

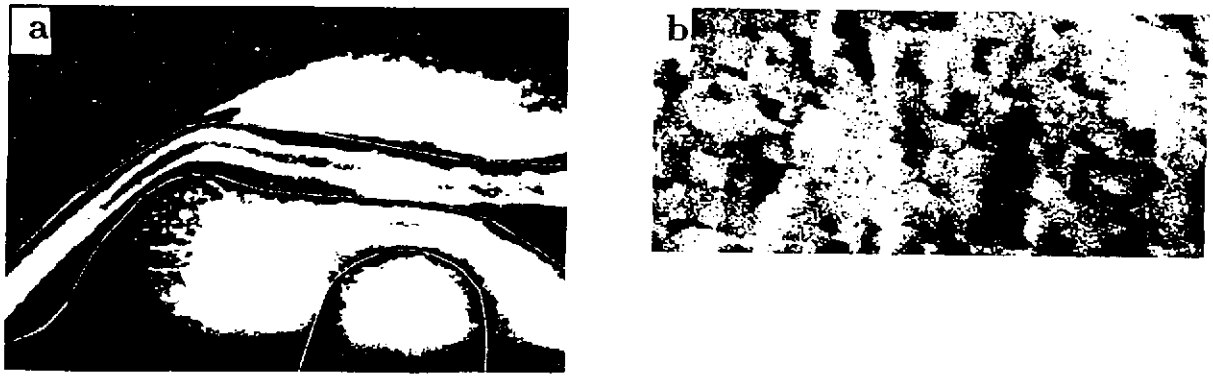

Figure 12. Topograms of $LiNbO_3$ samples. (a) 1:1. Different parts of the crystal reflecting at a slightly different angle of incidence. Four topograms have been put together to show different reflecting parts of the crystal. (b) 66x magnified.

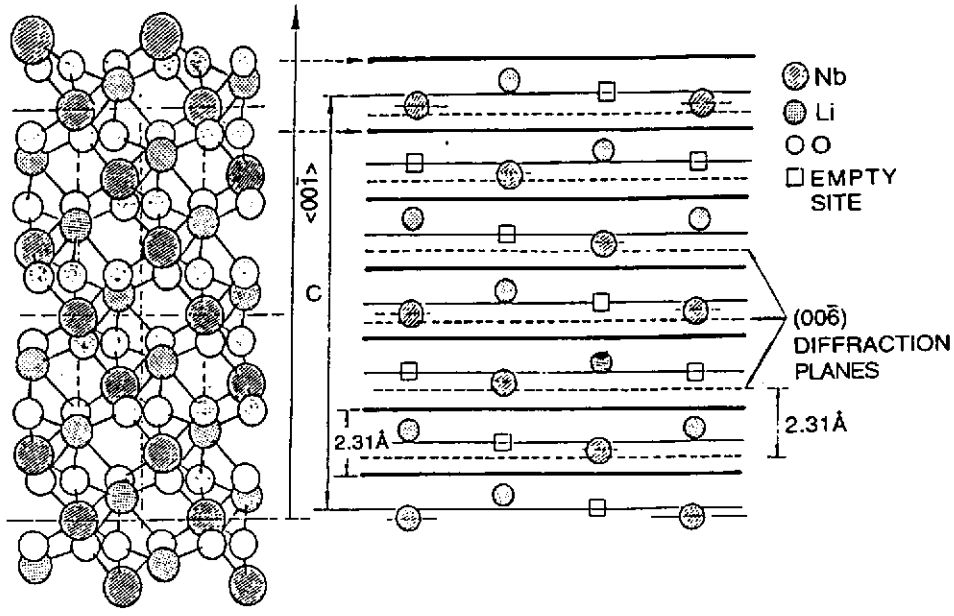

Figure 13. Structure of $LiNbO_3$ showing the positions of the $(00\bar{6})$ diffraction planes.

Figure 14 shows the (006) and the $(00\bar{6})$ reflectivities and corresponding Nb L fluorescence yields for an incident x-ray energy of 8.3 keV. For the (006) case the reflectivity is higher compared to $(00\bar{6})$ and the corresponding normalized fluorescence yield is lower. This is what is expected as shown in the theoretical plots for several energies in Figures 6 and 7. At 8.3 keV for Si(220) the Bragg angle is 22.90°. The asymmetry angle φ of the asymmetrically cut Si(220) monochromator crystal was 20°. This gives b = -

0.074. The width of the reflectivity curve for a symmetrically cut silicon crystal for (220) reflection is 24.2 μrad (5 arc sec.). Thus the divergence of the incident beam on the sample was 6.4 μrad (1.32 arc sec.). For $LiNbO_3$ (006) reflection, θ_B = 18.87° and the symmetrical reflection width is 24.7 μrad. Therefore, there is a slight broadening of the reflectivity curve because of dispersion and some smearing due to the finite angular width of the incident beam on the sample.

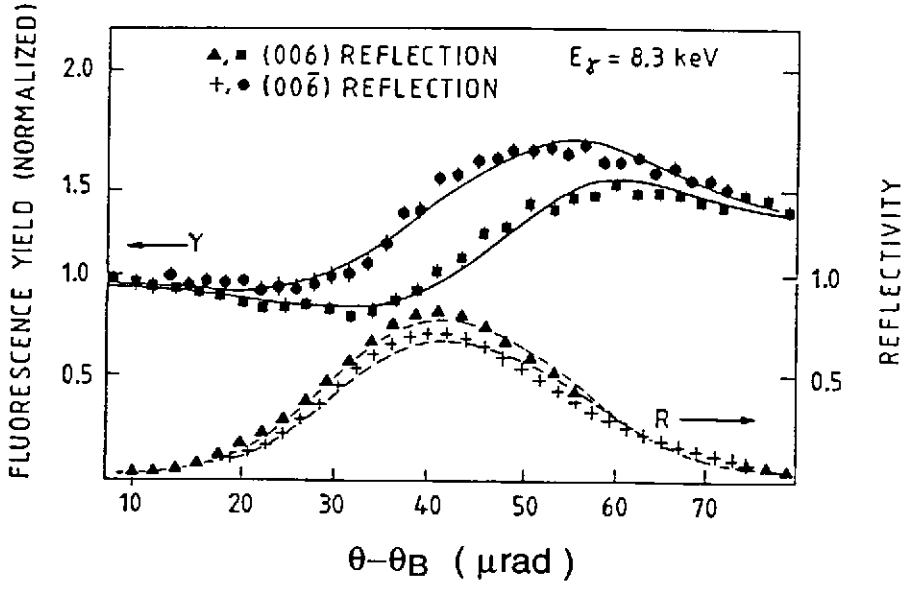

Figure 14. Reflectivity (+,▲) and Nb L fluorescence yield (● ,■) variation with the angle of incidence. Solid and dashed lines are theoretical fits.

The field intensities at the O site for (006) and (00$\bar{6}$) reflections were shown in Figure 7. The O position can be obtained by detecting O K_α fluorescence. For the low energy of the O K_α photons (525 eV) their absorption in air and in the Be window of the Si(Li) detector is very strong. However, if the sample is placed in a vacuum chamber and a windowless Si(Li) detector is used, O K_α photon detection would be simple. From this experiment one would directly get the relative positions of O atoms with respect to Nb atoms by analyzing both O K_α and Nb L signals.

Figure 15 shows the results of a measurement where, instead of detecting fluorescence photons, photoelectrons and Auger electrons have been detected. A typical electron yield spectrum is shown in Figure 16. In this experiment the sample was inside a gas flow proportional counter as detector[16,17] in which a flow of 90 % helium plus 10 % methane mixture was maintained. Photoelectrons and Auger electrons emitted from the sample ionize the gas resulting in a cascade which is collected at a 50 μm thin gold-coated tungsten

wire kept at a high voltage (≅ + 1000 V). The efficiency of the chosen gas mixture is very high for ionization by keV electrons and very small (≤ 1 %) for keV photons. The whole detector containing the sample was mounted on an Eulerian cradle with a special stage for standing wave experiments. The electron spectra were collected in a multichannel analyzer.

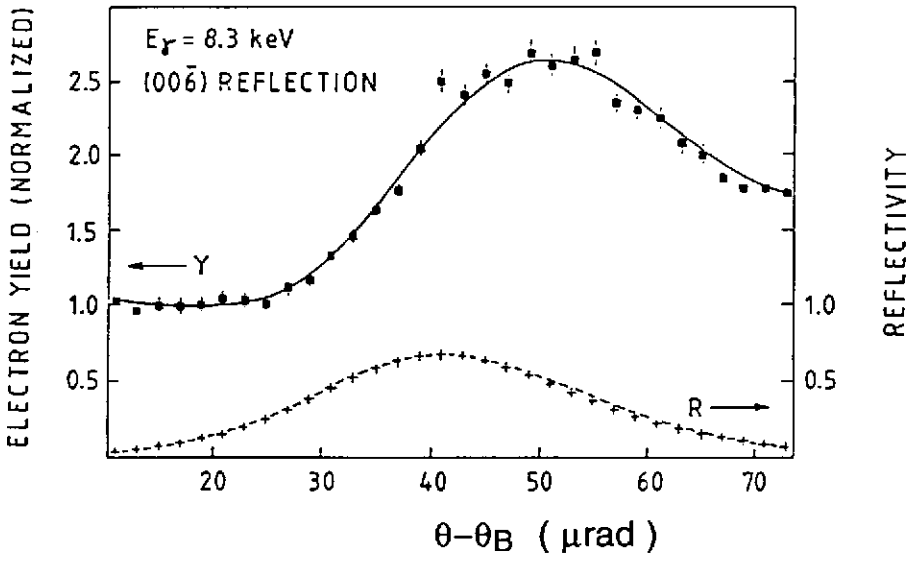

Figure 15. Reflectivity (+) and the Nb L photoelectron yield (■) variation with respect to the angle of incidence. Dashed and solid lines are theoretical fit.

Around a photon energy of 8 keV, we roughly estimate from Refs. 18 and 19 the ratio of the photoionization cross sections to be σ_L(Nb) : σ_M(Nb) : σ_K(O) : σ_K(Li) = 4.4×10^3 : 7.3×10^2 : 6.6x10 : 1. Therefore, in the spectrum of Figure 16 the contribution from electrons originating from O and Li is negligible and the dominant photoelectron contribution is from Nb L shell ionization. Also, in this case, after photoionization, the atomic deexcitation occurs predominantly[20] by Auger electron emission. The spectrum thus shows two main peaks. At 8.3 keV incident energy, Nb L photoelectrons have energies of 5.93, 5.84 and 5.59 keV corresponding to transitions from L_{III}, L_{II} and L_I edges, Nb(LMM) Auger electrons in the range 2.1-2.3 keV and Nb M photoelectrons around 8 keV. In Figure 15, the electron yield over a fixed region of channel numbers at the Nb(L) photoelectron peak from the 32 electron yield spectra has been plotted.

At this point let us compare the results obtained by the detection of NbK_α (Figure 17) and Nb L fluorescence photons in the light of crystal perfection. When the high energy Nb K_α photons (16.58 keV) are detected, one is probing a larger depth of the sample compared to when the low energy Nb L photons

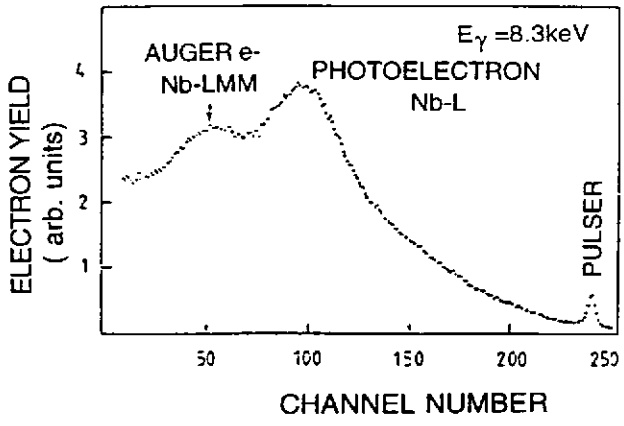

Figure 16. An electron energy spectrum from a $LiNbO_3$ sample detected by a gas proportional counter detector in which the sample is built-in.

(2.16-2.26 keV) are detected. z_{eff} ($\eta' = 0$) is 0.736 μm and 628 Å for Nb Kα and Nb L photons, respectively, for $\alpha = 1°$. For the Nb L photons even at $\alpha = 50°$ Z_{eff} ($\eta' = 0$) is 0.687 μm. These values are obtained from Eq. (2.37)-(2.43). From the detailed analysis one can determine the degree of disorder in the sample. In the present case a larger degree of disorder for the measurement with Nb L fluorescence indicated that more disorder was left in the surface region from inadequate polishing of the sample.

5. CONCLUSIONS

In this article we have discussed that x-ray standing waves are formed inside large perfect crystals when a diffraction condition is satisfied. As the angle of incidence advances across the rocking curve the antinodes of the x-ray standing wave move inward and eventually get fixed at a particular position with respect to the atomic coordinates in the unit cell. This position is identified to be the position of a diffraction plane. The antinodal planes have the same periodicity as the periodicity of the diffraction planes. When the incident energy of the x-ray beam is just near an absorption edge, the anomalous dispersion parameters f' and f'' undergo strong changes compared to their values when the incident pnoton energy is far away from the edge. The changes in f' and f'' in turn change the phases of the structure factors. The value of the structure factor phase decides the position of the diffraction planes, which can be measured in x-ray standing wave experiments by detecting and analyzing an inelastic signal, such as fluorescence, photoelectrons or Auger electrons generated at a particular type of atoms in the crystal while the crystal is diffracting. Under a diffraction condition most of the photons undergo elastic scattering. However, a small fraction of photons always undergoes inelastic interaction, which is sufficient for the measurements to determine the phase of the structure factors.

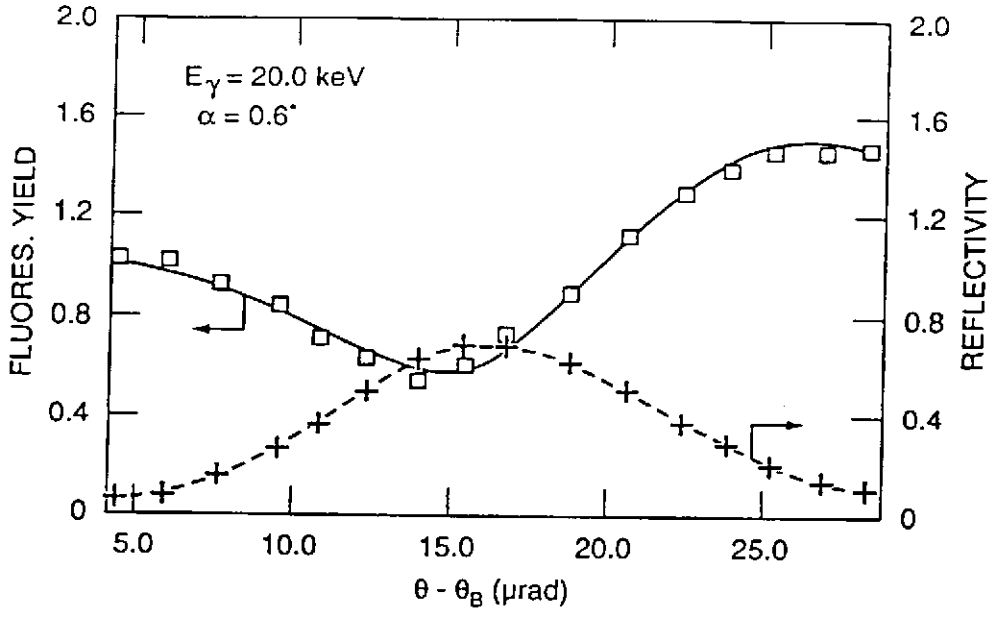

Figure 17. Reflectivity (+) and $Nb\,K_\alpha$ fluorescence yield (□) for E_γ = 20.0 keV. Solid and dashed lines are theoretical fit. The results are for the (006) reflection.

With the semiforbidden GaAs(200) reflection, phase variation over a wide region near the absorption edges have been demonstrated. A noncentrosymmetric crystal $LiNbO_3$ containing a large number of defects, dislocations and strain with a reasonably large unit cell (30 atoms) have been used to demonstrate the generality of the x-ray standing wave method for phase determination. Again, the effect of anomalous scattering on the reflectivity and the angular yield profile of the inelastic signals have been explained in terms of the phase of the structure factor.

It is known that congruent $LiNbO_3$ crystals have antisite defects - about 6 % Nb atoms at the Li site. A quantitative estimate of the antisite defects can be obtained from the measured phase of the standing wave field. For $LiNbO_3$ 6 % Nb atoms at the Li site introduces a 1.7 % shift in the standing wave phase, which is easily detected.

$LiNbO_3$ also offers a very interesting situation. When the c-axis is parallel to the surface, this crystal exhibits a rotation of x-ray polarization [21]. Therefore the standing wave field will be determined by a mixed polarization state, even when the incident beam is 100 % σ or π polarized. The absorption of x-rays also depends on the relative angle between the c-axis and the polarization direction of the incident beam. The anisotropies are quite strong around the Nb K edge. Recently, in hematite (α-Fe_2O_3) crystals (space group $(R\bar{3}c)$ a fiftyfold enhancement in the diffracted signal for a forbidden reflection was observed at an incident x-ray energy of 10 eV below the iron K edge. Hematite also exhibited a rotation of polarization [22]. X-ray standing wave studies in these cases would be interesting. Some systems like hematite

would offer the possibility of studying the magnetic effect simultaneously. A measurement of the magnetic effect excited by a standing wave field has already been reported [23].

6. REFERENCES

1 C.G. Darwin, Phil. Mag. 27, 315 (1914); 27, 675 (1914).
2 P.P. Ewald, Ann. Physik 49, 1 (1916); 49, 117 (1916); 54, 519 (1917); Acta Crysta. 11, 888 (1958).
3 M.v. Laue, Ergeb. Exakt. Naturw. 10, 133 (1931); "Röntgenstrahl-Interferenzen" (Akademischer Verlag, Frankfurt, 1960).
4 Z.G. Pinsker, "Dynamical Scattering of X-rays in Crystals" (Springer-Verlag, Berlin, 1978).
5 W.H. Zachariasen, "Theory of X-ray Diffraction in Crystals" (John Wiley & Sons, Inc., New York, 1945).
6 R.W. James, "The Optical Principles of the Diffraction of X-rays" (G. Bell and Sons, London, 1950).
7 B.W. Batterman and H. Cole, Rev. Mod. Phys. 36, 681 (1964).
8 M.J. Bedzyk and G. Materlik, Phys. Rev. B32, 6456 (1985).
9 D.T. Cromer and D. Liberman, J. Chem. Phys. 53, 1891 (1970).
10 Estimated from the temperature factors given in Ref. 12.
11 U. Bonse and E. Kappler, Z. Naturforschung 13A, 792 (1958).
12 S.C. Abrahams, J.M. Reddy and J.L. Bernstein, J. Phys. Chem. Solids 27, 997 (1966).
13 S.C. Abrahams, W.C. Hamilton and J.M. Reddy, J. Phys. Chem. Solids 27, 1013 (1966); S.C. Abrahams, H.J. Levinstein and J.M. Reddy, J. Phys. Chem. Solids 27, 1019 (1966).
14 S.C. Abrahams and P. Marsh, Acta Cryst. B42, 61 (1986).
15 I. Fujimoto, Phys. Rev. Lett. 40, 941 (1978).
16 N. Hertel, M.V. Kovalchuk, A.M. Afanesev and R.M. Imanov, Phys. Lett. 75A, 501 (1980).
17 M.J. Bedzyk, G. Materlik and M.V. Kovalchuk, Phys. Rev. B30, 2453 (1984).
18 J.J. Yeh and I. Lindau, Atomic and Nuclear Data Tables 32, 1 (1985).
19 E. Storm and H.I. Israel, Nuclear Data Tables A7, 565 (1970).
20 M.O. Krause, J. Phys. Chem. Ref. Data 8, 307 (1979).
21 A. Kirfel, this book.
22 K.D. Finkelstein, Qun Shen and S. Shastri, Physical Review Letters 69, 1612 (1992)
23 H. Kawata, T. Iwazumi, N. Shiotani and F. Itoh, in this book.